

Mapping the magnetization fine structure of a lattice of Bloch-type skyrmions in an FeGe thin film

András Kovács,^{1(a)} Jan Caron,¹ Andrii S. Savchenko,² Nikolai S. Kiselev,^{3(b)} Kiyou Shibata,⁴ Zi-An Li,⁵ Naoya Kanazawa,⁶ Yoshinori Tokura,^{4,6} Stefan Blügel,³ and Rafal E. Dunin-Borkowski¹

¹Ernst Ruska-Centre for Microscopy and Spectroscopy with Electrons and Peter Grünberg Institute, Forschungszentrum Jülich, 52425 Jülich, Germany

²Donetsk Institute for Physics and Engineering, National Academy of Sciences of Ukraine, 03028 Kyiv, Ukraine

³Peter Grünberg Institute and Institute for Advanced Simulation, Forschungszentrum Jülich and JARA, 52425 Jülich, Germany

⁴RIKEN Center for Emergent Matter Science (CEMS), Wako 351-0198, Japan

⁵Institute of Physics, Chinese Academy of Sciences, 100190 Beijing, China

⁶Department of Applied Physics, The University of Tokyo, Tokyo 113-8656, Japan

(Received 12 September 2017; accepted 10 October 2017; published online 8 November 2017)

Bloch-type magnetic skyrmions are nanoscale vortex-like spin objects that form densely packed lattice arrangements in *B20*-type chiral magnets in the presence of a magnetic field. Here, we use off-axis electron holography, in combination with an iterative model-based reconstruction algorithm, to study the geometries of the projected in-plane magnetization distributions of individual skyrmions in an FeGe thin film as a function of applied magnetic field. We compare our results with micromagnetic simulations and find a departure from magnetic chirality in the transition regions between adjacent skyrmions when they are in lattice arrangements. © 2017 Author(s). All article content, except where otherwise noted, is licensed under a Creative Commons Attribution (CC BY) license (<http://creativecommons.org/licenses/by/4.0/>). <https://doi.org/10.1063/1.5004394>

Magnetic skyrmions are topologically protected spin textures that are attracting considerable attention due to their interesting physical properties and potential applications in energy-efficient spintronic devices for information technology.^{1,2} Particular interest in magnetic skyrmions arose after the discovery of their current-induced motion at very low current densities,³ suggesting that they could be used as building blocks in new generations of recording media. The spin structure of a magnetic skyrmion originates from the Dzyaloshinskii-Moriya interaction (DMI), a strong spin-orbit interaction that appears in crystals with broken inversion symmetry, including *B20*-type structures,⁴ as well as at interfaces in thin magnetic films.⁵ In thin films of *B20* chiral magnets, a regular hexagonal skyrmion lattice (SkL) of Bloch-type skyrmions is formed in the presence of a small magnetic field applied parallel to the surface normal direction.⁶

Experimental observations of magnetic skyrmions were first made using neutron diffraction.⁴ Subsequently, several different phase contrast techniques in the transmission electron microscope (TEM) have been used to image skyrmions in real space. The phase shift of the electron wave that has passed through a sample in the TEM can be expressed in the following form:

$$\phi(x, y) = C_E \int V_0(x, y, z) dz - \frac{e}{\hbar} \int A_z(x, y, z) dz, \quad (1)$$

where x and y are directions in the plane of the sample, z is the incident electron beam direction, C_E is an interaction

constant ($6.53 \times 10^6 \text{ rad V}^{-1} \text{ m}^{-1}$ at an accelerating voltage of 300 kV), V_0 is the mean inner potential of the sample, e is the electron charge, \hbar is the reduced Planck constant, and A_z is the component of the magnetic vector potential \mathbf{A} along z . The Fresnel mode of Lorentz TEM,^{7,8} which has been used to identify the formation of skyrmions and to follow their dynamics,^{9,10} records a signal that is approximately proportional to the second derivative of the phase. Differential phase contrast (DPC) imaging¹¹ in the scanning TEM, which has been used to image a magnetic SkL at a domain boundary in *B20*-type FeGeSi¹² and to study the internal structures of skyrmions,¹³ records a signal that is approximately proportional to the first derivative of the phase. Off-axis electron holography¹⁴ (EH) provides direct access to the phase shift with high spatial resolution and high phase sensitivity. The technique has previously been applied to study the structures of helical and skyrmion phases in *B20*-type FeCoSi¹⁵ and the internal and lattice structure of skyrmions in FeGe as a function of applied magnetic field and temperature.¹⁶

All phase contrast techniques in the TEM are sensitive to the projected in-plane components of the magnetic induction $\mathbf{B} = \mu_0(\mathbf{H} + \mathbf{M}) = \nabla \times \mathbf{A}$ inside and outside the specimen, where \mathbf{M} is the magnetization, \mathbf{H} is the auxiliary (or demagnetizing) field, and μ_0 is the permeability in vacuum. Until now, only the measurement and mapping of the projected in-plane components of the \mathbf{B} -field was possible and the \mathbf{M} -field was not accessible. Recently, we developed an iterative model-based algorithm, which can be used to determine the in-plane magnetization M_{xy} , projected along the z direction, from the magnetic contribution to the phase ϕ_M recorded using off-axis EH by making use of a discretized

^{a)}Electronic mail: a.kovacs@fz-juelich.de

^{b)}Electronic mail: n.kiselev@fz-juelich.de

numerical implementation of a forward model based on trial solutions for the magnetization. A short description of the approach is given in the [supplementary material](#).

Here, we study the shapes and fine structures of Bloch-type skyrmions in *B20*-type FeGe thin films using off-axis EH. We determine the projected in-plane magnetization M_{xy} of individual skyrmions from electron-optical magnetic phase images and compare our results with micromagnetic simulations. Our measurements of magnetization allow local variations in skyrmion shape and core diameter with applied magnetic field, as well as the magnetic texture in inter-skyrmion regions, to be determined quantitatively.

Single crystalline *B20*-type FeGe was synthesized using a chemical vapor transport method.¹⁷ A 100-nm-thick lamella with a $\langle 110 \rangle$ surface normal was prepared for TEM examination by focused ion beam milling with Ga⁺ ions using a dual-beam scanning electron microscope (Hitachi NB 5000). Off-axis electron holograms were recorded using a positively charged biprism in an image spherical aberration (C_s) corrected FEI Titan 60–300 TEM operated in Lorentz mode at an accelerating voltage of 300 kV. With the C_s of approximately 0.2 mm, the point resolution in Lorentz mode is estimated to be 1 nm. The electron holograms were recorded with a fringe spacing of 2.4 nm, a fringe contrast of 15 %, resulting in a spatial resolution of the reconstructed phase of 7.2 nm, and a phase resolution of 0.15 rad. A pre-calibrated out-of-plane magnetic field was applied to the sample during off-axis EH using the conventional microscope objective lens. The magnetic contribution to the phase [the second term in Eq. (1)] was separated from the mean inner potential contribution [the first term in Eq. (1)] by taking the difference between phase images recorded at 200 K and at room temperature, when FeGe is non-magnetic ($T_c^{\text{FeGe}} = 278.7 \text{ K}$), on the assumption that there are no changes in diffraction contrast, specimen charging, or mean inner potential between the two temperatures.

Figure 1 shows experimental magnetic phase images of skyrmions in FeGe for different values of the magnetic field applied parallel to the electron beam direction. The sample was field-cooled in the presence of a 100 mT magnetic field to 95 K in order to generate a SkL and then heated to 200 K. The SkL did not form a perfect arrangement but contained a dislocation, whose core is marked in Fig. 1(a). The presence of the dislocation results in local geometrical changes to skyrmion shape, as reported recently using off-axis EH.¹⁸ As the applied magnetic field is increased, the hexagonal SkL changes progressively to a more random distribution of individual skyrmions, as shown in Figs. 1(b) and 1(c). The distance between adjacent skyrmions increases with applied magnetic field, until they are eliminated in the saturated ferromagnetic state. The magnetic field dependence of the internal structures of skyrmions is described in detail in Ref. 16. The step in the magnetic contribution to the phase between the centre and the edge of each skyrmion for the present specimen thickness is measured to be approximately 0.6 rad. A color-contour map, which was generated directly from a magnetic phase image and provides a visual representation of the projected in-plane magnetic induction, is shown in Fig. 1(d). The magnetic field of the skyrmions rotates counterclockwise.¹⁹ The measured saturation magnetization is

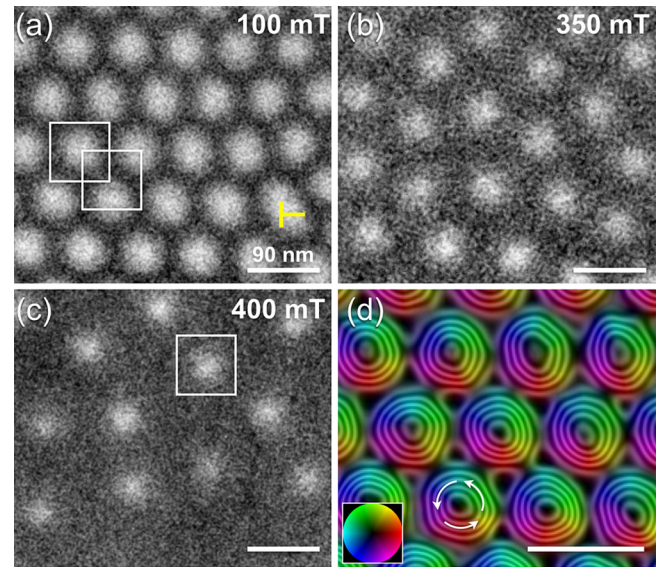


FIG. 1. Experimental magnetic phase images recorded using off-axis EH, showing magnetic skyrmions in *B20*-type FeGe at 200 K in the presence of externally applied magnetic fields of (a) 100, (b) 350, and (c) 400 mT. In (a), the SkL is distorted slightly as a result of the presence of a dislocation core (marked). The skyrmions that are marked by squares in (a) and (c) are analyzed further in Figs. 2 and 3. (d) Magnetic induction map (color coded contour plot) of a SkL at 100 mT determined from a magnetic phase image showing counterclockwise magnetic field rotation. The contour spacing is $2\pi/64 = 0.098$ rad. The scale bar is 90 nm.

approximately 100 kA m^{-1} at 200 K, which is somewhat lower than the expected value²⁰ of 384 kA m^{-1} at 0 K, although other experimental studies have also reported reduced magnetization values for FeGe thin films.^{21,22} The difference is likely to be due to the temperature of 200 K used in our experiment, the surface chiral twist of the spin structure of each skyrmion, the presence of a non-magnetic surface layer resulting from specimen preparation and possible inaccuracy in the determination of the specimen thickness.

Individual skyrmions from the SkL and the random skyrmion distribution were selected for analysis by determining M_{xy} from the recorded magnetic phase ϕ_M using the model-based iterative algorithm, as shown in Fig. 2. The resulting maps of the magnitude of M_{xy} in Fig. 2 reveal that at 100 mT the skyrmions in a SkL have hexagonal shapes, while at 400 mT they have circular shapes. A shear in the hexagonal skyrmion shape by approximately 5 nm results from the presence of the dislocation in the planar skyrmion arrangement, as marked in Fig. 1(a). The distance between the dislocation core and the chosen skyrmion is approximately 250 nm, highlighting the extent of the distortion in the skyrmion lattice and the flexibility of the skyrmion shape. As the magnetic field is increased, the skyrmion core diameter decreases from 13.3 nm in the SkL to 9.5 nm in individual skyrmions, in agreement with theoretical predictions²³ and previous experimental observations.^{13,16}

Figures 3(a) and 3(b) show the magnitude of the projected in-plane magnetization and a corresponding vector map for an inter-skyrmion region in the SkL. Intensity line-scans between neighboring skyrmions are shown in Figs. 3(c) and 3(d). Unexpected peaks in the magnetization distribution are visible in Fig. 3(d).

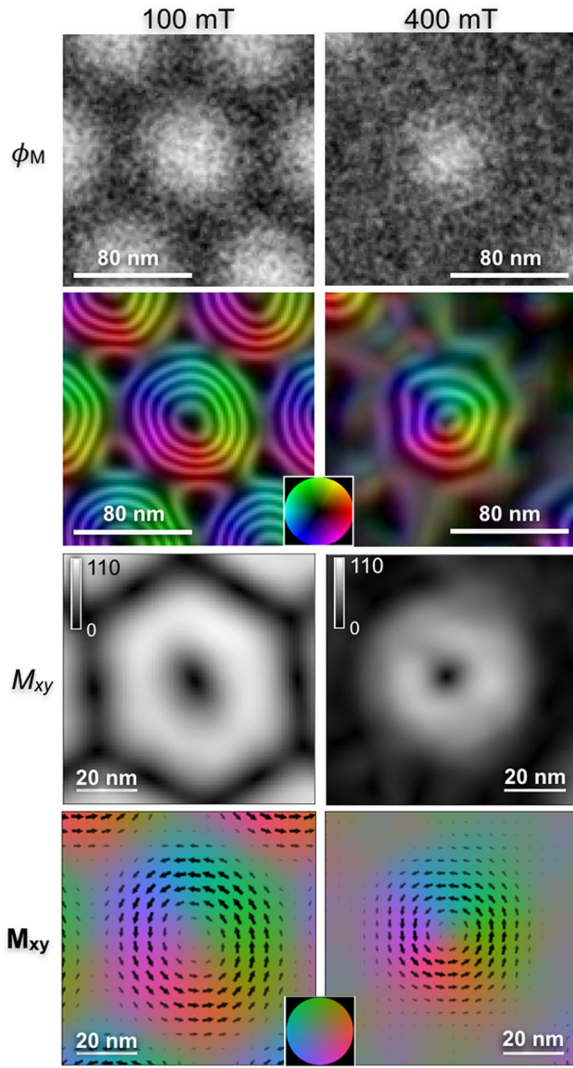


FIG. 2. Determination of the magnetic properties of individual skyrmions at 100 and 400 mT. The row labeled ϕ_M shows experimental magnetic phase images recorded using off-axis EH. The row below ϕ_M shows magnetic induction (color-contour) maps determined from the magnetic phase images (the contour spacing is $2\pi/64 = 0.098$ rad). The row labeled M_{xy} shows the magnitude of the projected in-plane magnetization determined from ϕ_M using an iterative model-based reconstruction algorithm. The row labeled \mathbf{M}_{xy} shows color-coded vector maps of the projected in-plane magnetization. M_{xy} is displayed in units of kA m^{-1} .

The experimental results were compared with a classical micromagnetic model for an isotropic chiral magnet that includes the following energy terms: the Heisenberg exchange interaction, the DMI, the interaction with the applied field (the Zeeman term), and the interaction with the demagnetizing field, in the form

$$\mathcal{E} = \int_{V_s} \left\{ \mathcal{A} \left(\partial_x \hat{m}^2 + \partial_y \hat{m}^2 + \partial_z \hat{m}^2 \right) + \mathcal{D} \hat{m} \cdot [\nabla \times \hat{m}] + M_s \mathbf{B}_{\text{ext}} \cdot \hat{m} - \frac{1}{2} M_s \mathbf{B}_d \cdot \hat{m} \right\} dr, \quad (2)$$

where the integration extends over the volume V_s of the sample, $\hat{m} \equiv \hat{m}(x, y, z)$ is a continuous unit vector field $\hat{m} = \mathbf{M}/M_s$, and the saturation magnetization of B20-type FeGe $M_s = 384 \text{ kA m}^{-1}$. In Eq. (2), \mathbf{B}_{ext} is the externally applied magnetic field and \mathbf{B}_d is the demagnetizing field generated

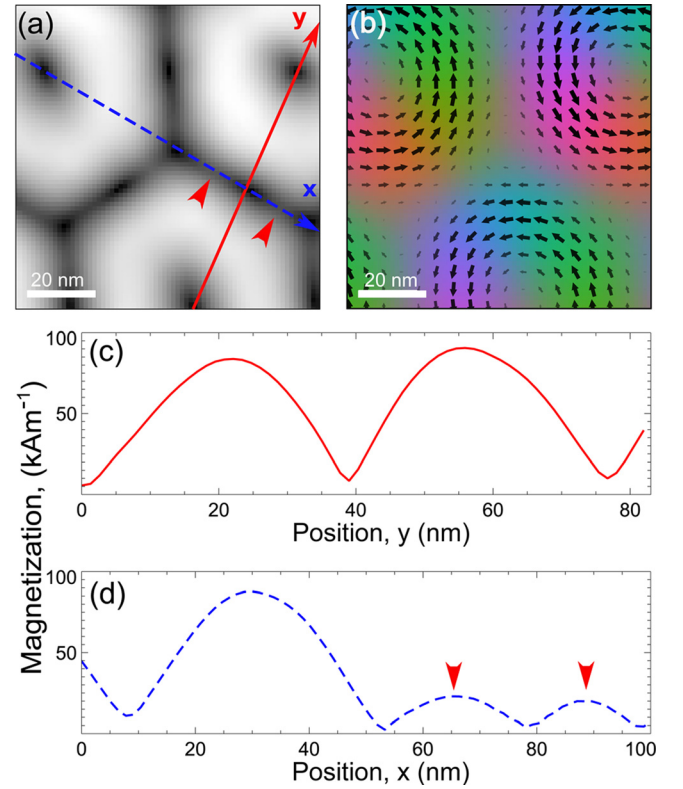


FIG. 3. (a) Magnitude and (b) vector map of the projected in-plane magnetization distribution in a SkL measured using off-axis EH. The blue and red lines in (a) mark the positions of the linescans plotted in (c) and (d), respectively. The blue and red lines join distant and nearest skyrmion neighbours, respectively. Maxima in (a) and (d) are marked by small arrows.

by the divergence of the magnetization in the sample and at its surface. The simulations were performed using MuMax3.²⁴ For a correct description of the demagnetizing field, we used periodic boundary conditions with a repetition of the simulated domain in the x and y directions, in order to describe the extended film.¹⁶ The values of micromagnetic exchange stiffness $\mathcal{A} = 8.78 \text{ pJ/m}$ and DMI constant $\mathcal{D} = 1.576 \text{ mJ/m}^2$ were chosen to fit the experimentally measured value of the equilibrium period of the helical spin spiral L_D in FeGe of 70 nm, according to the well-known analytical expression $L_D = 4\pi\mathcal{A}/\mathcal{D}$. The equilibrium period of a hexagonal unit cell of the SkL, corresponding to the lowest energy density, was found by direct energy minimization using the method of conjugate gradients implemented in MuMax3.

Figures 4(a) and 4(b) show the simulated magnetization distribution within the hexagonal unit cell and the projected magnetization averaged through the film thickness, respectively. Line profiles of the magnetization along the directions marked in Fig. 4(b) are shown in Figs. 4(c) and 4(d). In the line profile shown in Fig. 4(c), which joins neighboring skyrmions, the chain of spins exhibits a Bloch-like domain wall with a fixed right-handed vorticity. Remarkably, in Fig. 4(d), the vorticity of the transition region between more distant skyrmions shows a violation of chirality. In between the points that are indicated by red arrows, the modulation has a left-handed vorticity. Figures 4(e) and 4(f) show the values of the simulated in-plane component of the average magnetization between the skyrmions along the two orthogonal

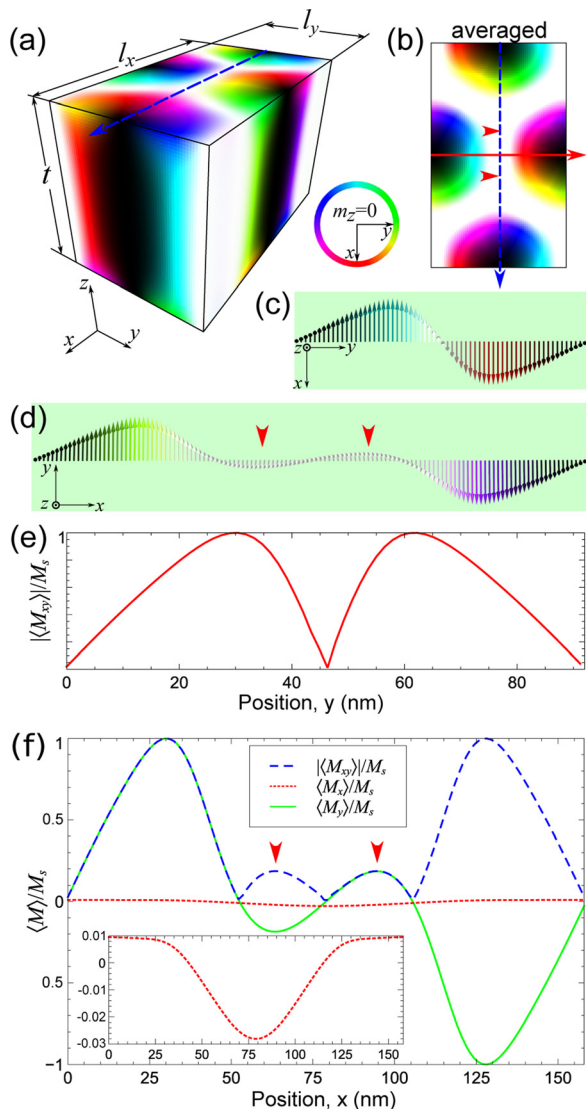


FIG. 4. Results of micromagnetic simulations for a 100-nm-thick $B20$ -type FeGe thin film. (a) Magnetization within a simulated domain that matches the period of a skyrmion lattice in an applied magnetic field of $\mathbf{B}_{\text{ext}} = 100$ mT. (b) Average magnetization projected onto the xy plane. (c) and (d) Magnetization along the red and blue lines in (b), respectively. (e) and (f) In-plane components of the magnetization corresponding to (c) and (d), respectively. The red arrows indicate the positions of maxima between skyrmions along the blue line.

directions in the hexagonal SkL indicated in Figs. 4(a) and 4(b). The $|\langle M_{xy} \rangle|/M_s$ component [Fig. 4(e)] is in a good agreement with the experimentally measured in-plane magnetization (Fig. 3). This behavior can be explained by a competition between different energy terms, which are associated with a local decrease in energy due to the DMI, and result in a reduction in the total energy of the system. A detailed analysis of such an interplay between energy terms, supported by a visualization of DMI and exchange energy density maps within a skyrmion unit cell, has been presented in Ref. 13. In the present study, such a non-trivial character of the modulation within the skyrmion lattice is responsible for the appearance of two maxima in the projected in-plane magnetization shown in Fig. 4(f). The observed peaks are only approximately 20% of the height of the maximum in the line profile and could not have been identified or measured readily from standard Lorentz TEM images. Intensity

analyses of Lorentz TEM images are given in the [supplementary material](#).

In summary, we have measured and interpreted the local magnetization distribution in a lattice of Bloch-type skyrmions in a $B20$ -type FeGe thin film using off-axis electron holography, in combination with the use of a model-based inversion algorithm and micromagnetic simulations. Skyrmions in a close-packed honeycomb lattice possess a hexagonal magnetization distribution that is sensitive to the presence of lattice defects. Upon magnetic field saturation, the skyrmion lattice breaks down into a random distribution of skyrmions that have circular shapes and reduced core diameters. The magnetization distribution in the interstitial region between adjacent skyrmions in a lattice arrangement shows a Bloch-wall-type transition between neighboring skyrmions. Between more distant skyrmions, the magnetization distribution shows a more complex modulation with a change in chirality. This newly resolved magnetic fine structure raises questions about the magneto-transport properties of electrons in skyrmion lattices. Off-axis electron holography combined with magnetization calculations provides a high spatial resolution, quantitative technique for the measurement of local magnetic properties.

See [supplementary material](#) for the description of the model-based iterative reconstruction method and for the image intensity analysis of Lorentz defocused images.

R.D.-B., J.C., A.S., and A.K. are grateful to the European Research Council for financial support under the European Union's Seventh Framework Programme (FP7/2007-2013)/ERC Grant Agreement No. 320832. K.S., N.K., and Y.T. acknowledge financial support from the Grant-in-Aid for Scientific Research (Grant Nos. 24224009 and 14J09358) from MEXT and the FIRST Program in Japan. K.S. was supported by the Japan Society for the Promotion of Science through a Program for Leading Graduate Schools (MERIT). A.S. is grateful for support from the Ukrainian State Fund for Fundamental Research (Project No.: F71/59-2017). Z.-A. L. acknowledges the financial support from the NSF of China (No.11774403).

¹N. S. Kiselev, A. N. Bogdanov, R. Schäfer, and U. K. Rössler, *J. Phys. D: Appl. Phys.* **44**, 392001 (2011).

²A. Fert, V. Cros, and J. Sampaio, *Nat. Nanotechnol.* **8**, 152 (2013).

³X. Z. Yu, N. Kanazawa, W. Z. Zhang, T. Nagai, T. Hara, K. Kimoto, Y. Matsui, Y. Onose, and Y. Tokura, *Nat. Commun.* **3**, 988 (2012).

⁴S. Mühlbauer, B. Binz, F. Jonietz, C. Pfleiderer, A. Rosch, A. Neubauer, R. Georgii, and P. Böni, *Science* **323**, 915 (2009).

⁵S. Heinze, K. von Bergmann, M. Menzel, J. Brede, A. Kubetzka, R. Wiesendanger, G. Bihlmayer, and S. Blügel, *Nat. Phys.* **7**, 713 (2011).

⁶X. Z. Yu, N. Kanazawa, Y. Onose, K. Kimoto, W. Zhang, S. Ishiwata, Y. Matsui, and Y. Tokura, *Nat. Mater.* **10**, 106 (2011).

⁷X. Z. Yu, Y. Onose, N. Kanazawa, J. H. Park, J. H. Han, Y. Matsui, N. Nagaosa, and Y. Tokura, *Nature* **465**, 901 (2010).

⁸H. Du, R. Che, L. Kong, X. Zhao, C. Jin, C. Wang, J. Yang, W. Ning, R. Li, C. Jin, X. Chen, J. Zang, Y. Zhang, and M. Tian, *Nat. Commun.* **6**, 8504 (2015).

⁹J. Rajeswari, P. Huang, G. F. Mancini, Y. Murooka, T. Latychevskaia, D. McGrouther, M. Cantoni, E. Baldini, J. S. White, A. Magrez, T. Giamarchi, H. M. Rønnow, and F. Carbone, *Proc. Natl. Acad. Sci. U.S.A.* **112**, 14212 (2015).

¹⁰X. Zhao, C. Jin, C. Wang, H. Du, J. Zang, M. Tian, R. Che, and Y. Zhang, *Proc. Natl. Acad. Sci. U.S.A.* **113**, 4918 (2016).

- ¹¹S. McVitie, D. McGrouther, S. McFadzean, D. MacLaren, K. OShea, and M. Benitez, *Ultramicroscopy* **152**, 57 (2015).
- ¹²T. Matsumoto, Y.-G. So, Y. Kohno, H. Sawada, Y. Ikuhara, and N. Shibata, *Sci. Adv.* **2**, 1501280 (2016).
- ¹³D. McGrouther, R. J. Lamb, M. Krajnak, S. McFadzean, S. McVitie, R. L. Stamps, A. O. Leonov, A. N. Bogdanov, and Y. Togawa, *New J. Phys.* **18**, 095004 (2016).
- ¹⁴P. A. Midgley and R. E. Dunin-Borkowski, *Nat. Mater.* **8**, 271 (2009).
- ¹⁵H. S. Park, X. Yu, S. Aizawa, T. Tanigaki, T. Akashi, Y. Takahashi, T. Matsuda, N. Kanazawa, Y. Onose, D. Shindo, A. Tonomura, and Y. Tokura, *Nat. Nanotechnol.* **9**, 337 (2014).
- ¹⁶K. Shibata, A. Kovács, N. S. Kiselev, N. Kanazawa, R. E. Dunin-Borkowski, and Y. Tokura, *Phys. Rev. Lett.* **118**, 087202 (2017).
- ¹⁷M. Richardson, *Acta Chem. Scand.* **21**, 2305 (1967).
- ¹⁸Z.-A. Li, F. Zheng, A. H. Tavabi, J. Caron, C. Jin, H. Du, A. Kovács, M. Tian, M. Farle, and R. E. Dunin-Borkowski, *Nano Lett.* **17**, 1395 (2017).
- ¹⁹K. Shibata, X. Z. Yu, T. Hara, D. Morikawa, N. Kanazawa, K. Kimoto, S. Ishiwata, Y. Matsui, and Y. Tokura, *Nat. Nanotechnol.* **8**, 723 (2013).
- ²⁰M. Beg, R. Carey, W. Wang, D. Cortés-Ortuño, M. Vousden, M.-A. Bisotti, M. Albert, D. Chernyshenko, O. Hovorka, R. L. Stamps, and H. Fangohr, *Sci. Rep.* **5**, 17137 (2015).
- ²¹N. A. Porter, J. C. Gartside, and C. H. Marrows, *Phys. Rev. B* **90**, 024403 (2014).
- ²²S. L. Zhang, I. Stasinopoulos, T. Lancaster, F. Xiao, A. Bauer, F. Rucker, A. A. Baker, A. I. Figueroa, Z. Salman, F. L. Pratt, S. J. Blundell, T. Prokscha, A. Suter, J. Waizner, M. Garst, D. Grundler, G. van der Laan, C. Pfleiderer, and T. Hesjedal, *Sci. Rep.* **7**, 123 (2017).
- ²³U. K. Röbler, A. A. Leonov, and A. N. Bogdanov, *J. Phys.: Conf. Ser.* **303**, 012105 (2011).
- ²⁴A. Vansteenkiste, J. Leliaert, M. Dvornik, M. Helsen, F. Garcia-Sanchez, and B. V. Waeyenberge, *AIP Adv.* **4**, 107133 (2014).